JOURNAL OF AIRCRAFT
Vol. 46, No. 1, January–February 2009

Experimental Analysis of Propeller–Wing Interactions for a Micro Air Vehicle

Brian J. Gamble* and Mark F. Reeder†
Air Force Institute of Technology, Wright–Patterson Air Force Base, Ohio 45433-7542

DOI: 10.2514/1.34520

An experimental investigation into the effects of the propeller slipstream on a small, flexible-wing air vehicle with a 24 in. wingspan was conducted at typical flight speeds, resulting in Reynolds numbers based on a mean aerodynamic chord of about 1×10^5. A static test bench was used to characterize the forces and moments acting on the motor and, separately, on the airframe. The motor and propeller, of diameter D, were mounted on a torque cell that was itself affixed to an air-bearing table configured to measure thrust. A model of the fuselage, capable of wing location adjustment, was affixed to a 6-degree-of-freedom balance. The resulting set of decoupled force and moment data was collected for axial wing placements ranging from 0.17 to 0.73 D and also for varied vertical wing placements. The results suggest that between 12 and 18% of propeller thrust translates into airframe drag, with the largest percentage occurring for the wing placement closest to the propeller (0.17 D). The measured reaction torque was found to be as high as 45% of the motor torque, and its dependence on wing placement was measured. Wind-tunnel data, collected using a six-component balance and a triaxial hot-wire anemometer mounted on a traversing system, yielded all three components of velocity maps for propeller-off and propeller-on conditions at typical operating airspeeds. The secondary flows generated by the propeller, propeller–wing interaction, and wing-tip vortices were captured and analyzed.

Nomenclature

b	=	wingspan
C_D	=	drag coefficient
C_L	=	lift coefficient
C_P	=	power coefficient
C_T	=	thrust coefficient
D	=	drag
l	=	roll moment
N	=	propeller rotational speed, revolutions per second
N_P	=	power number, $Q^*(2\pi N)/\rho N^3 D^5$
N_T	=	thrust number, $T/\rho N^2 D^4$
Q	=	propeller torque
R	=	propeller radius
Re_c	=	Reynolds number based on wing mean aerodynamic chord, $\rho V_\infty c/\mu$
Re_D	=	Reynolds number based on propeller diameter, $\rho N D^2/\mu$
T	=	thrust
u	=	axial velocity component
V_∞	=	freestream velocity
v	=	spanwise velocity component
w	=	vertical velocity component
X	=	streamwise direction in the tunnel
X_o	=	axial separation between propeller and wing
Y	=	lateral position in the tunnel
Z	=	vertical position in the tunnel
Z_o	=	vertical separation between propeller and wing
α	=	angle of attack
Γ	=	circulation
η	=	propeller efficiency
μ	=	viscosity
ρ	=	air density

Presented as Paper 3916 at the 36th AIAA Fluid Dynamics Conference and Exhibit, San Francisco, California, 5–8 June 2006; received 11 September 2007; revision received 25 January 2008; accepted for publication 10 February 2008.

*Captain, U.S. Air Force, Department. of Aeronautics and Astronautics, Building 640; currently at the Air Force Research Laboratory/Operations Integration Branch. Member AIAA.

†Assistant Professor, Department of Aeronautics and Astronautics, Building 640. Member AIAA.

I. Introduction

THE growth of interest in small unmanned air vehicles for a variety of military and civilian applications has been rapid over the past decade. These have been termed, alternatively, miniature air vehicles or micro air vehicles depending on their size and context. A wide variety of aircraft designs are under consideration, and propeller-driven aircraft are among the options. It is common for the propulsion system to be considered separately from the airframe, but the interaction between the propeller and the aerodynamic surfaces can affect aircraft stability, performance, energy consumption, and noise. The fact that the vehicles are small and unmanned leads to the placement of very different constraints on these miniature unmanned aircraft when compared with traditional designs. For example, there are applications for which a designer of a miniature air vehicle may be willing to sacrifice a level of stability to achieve a higher degree of maneuverability or to reduce the aircraft size. Additionally, the natural effect of lower Reynolds numbers associated with smaller vehicles generally becomes important in miniature air vehicles, and this can lead to dramatic differences in the aerodynamics from general aviation aircraft.

With these considerations in mind, the effects of propeller placement with respect to the airframe on performance and aircraft handling on miniature air vehicles warrant renewed consideration. Ideally, the air vehicle design must be stable and controllable while minimizing power consumption. Unfortunately, these are often conflicting requirements. For example, one way to improve directional stability might be to move the aircraft's center of gravity to a forward position. This, in turn, may require the center of gravity and the center of lift to shift forward to maintain a proper pitch moment for the aircraft. In turn, a reduced distance from the wing to the propeller might influence both propeller efficiency and the torque budget for the aircraft.

In the literature, there are two common experimental approaches to acquiring interaction data. One is to physically separate the power plant from the vehicle and acquire force and moment data for both propeller-driven fixed-wing aircraft and rotorcraft [1–4]. A second approach is to measure or computationally predict characteristics of

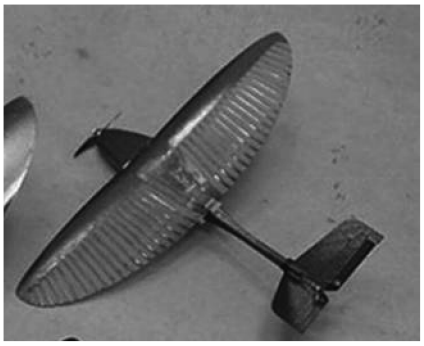

Fig. 1 The BATCAM vehicle.

the resulting pattern of velocities within the flowfield [5–9]. Each of the two approaches yields insight into the nature of the propeller–wing interaction and has its respective advantages and limitations. Force and moment measurements provide a single useful value in determining the end result of various configurations, whereas more intensive velocity measurements can yield insight into why a particular result occurs for a given geometry. One of the goals of this work is to use both types of tools to develop a better fundamental understanding of the propeller–airframe interference effects for a version of a specific air vehicle, the Battlefield Air Targeting Camera Autonomous Micro Air Vehicle (BATCAM). The BATCAM is shown in Fig. 1 and is described in more detail in [10]. A second goal of the study is to develop a better understanding of the influence of wing position relative to the propeller on the forces and moments acting on the aircraft.

II. Test Vehicle and Experimental Setup

The fuselage of the BATCAM is composed of a thin carbon fiber matrix, rectangular in shape and tapered back to a thin box-shaped tail boom. The wing, whether rigid or flexible, is mounted atop the fuselage. The control surfaces are ruddervators attached to a V-shaped tail. In all tests, the ruddervator angles were set to a 0 deg deflection. Although two types of wings, one nominally rigid and one nominally flexible, were used during the course of this study, the results given here are limited to those gathered for the flexible wing, which is more representative of the actual BATCAM vehicle. The wing geometries are described in an earlier work, and limited results gathered for the rigid design are described elsewhere [10,11]. The wing's leading-edge portion is rigid carbon fiber with carbon fiber ribs running the rest of the chord length of the wing. A flexible membrane is attached to the ribs to construct the rest of the wing. Table 1 lists the geometric properties of the basic aircraft configuration. The vehicle is designed to permit an interchange of propellers. However, only one propeller, a 6-in.-diam Graupner Super Nylon two-blade propeller with a pitch of 3 in., was used for all the tests reported here.

To perform a number of the propeller–wing interaction tests on the static test stand, a fuselage and separate wing mounting block were designed using SolidWorks® and built out of plastic using an Eden 3300 rapid prototype machine. This permitted the wing to be repositioned axially without changing the angle of attack of the wing. The basic dimensions of the fuselage were taken from the original vehicle, with some modifications. To ease the movement of the wing on the fuselage, the wing support stand was made with two pieces. The top portion followed the airfoil contour of the wing and was directly attached to the center of the wing. The bottom portion was shaped like the original fuselage with a flat top so that the wing portion could be repositioned. Tail effects were not studied using the static test apparatus, and the fuselage model ends just behind the trailing edge of the wing. A cylindrical hole is located at the rear of the fuselage for mounting on the sting and balance. A tongue-and-groove track system connects the fuselage model to the wing mounting block as shown in Fig. 2a. An offset top view of the static test apparatus with the wing placed in close proximity to the propeller is shown Fig. 2b. A schematic of the load measurement system for the static test setup is included in Fig. 2d.

Table 1 Geometric properties of the vehicle

Wing area	0.0605 m^2, (93.5 $in.^2$)
Root chord	0.15 m (6 in.)
Mean aerodynamic chord	0.107 m (4.2 in.)
Wingspan	0.61 m (24 in.)
Aspect ratio	6.16

A. Propeller–Wing Static Test

The purpose of this test was to separately measure the propeller torque and thrust along with the three forces and three moments acting on the wing in a static environment. To accomplish this, the motor and propeller were spaced apart from the aircraft. To provide the proper flow across the wing, an ElectriFly Model T-600R (7.2–9.6 V) reverse rotation electric motor was used and mounted opposite the front of the fuselage. The motor was mounted on a 350 N · mm (50 in. · oz) capacity Lebow Model 2105–50 torque cell with a nonlinearity of ±0.1% and a repeatability of 0.05% of full-scale capacity yielding an accuracy of 0.2 N · mm. Excitation of the torque cell was provided by a power supply and the signal was conditioned using a low-pass sixth-order Butterworth filter. The overhung load due to the weight of the motor was well within the specified moment limit (0.72 N · mm) and shear limit (89 N) of the torque cell. The torque cell was in turn mounted on a vertical bracket bolted to and spaced above the air-bearing table. A 111.2 N (25 lbf) capacity Interface load cell was placed at the opposite end of the air-bearing table and used to measure thrust. A very small preload provided the means to ensure repeatability, and a dead weight calibration was performed for both the torque cell and the load cell before testing. The Interface load cell has a nonlinear rating of 0.03% and a

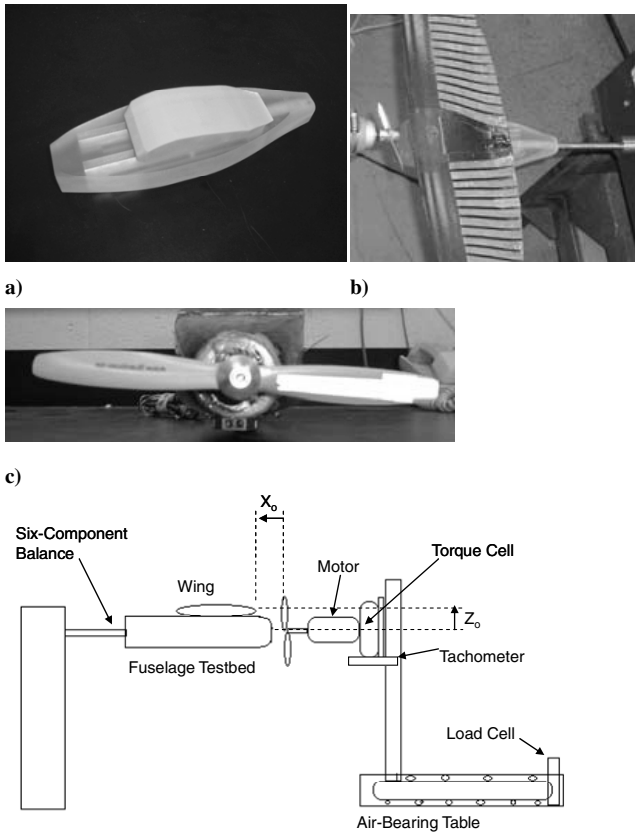

Fig. 2 Shown are the following: a) fuselage mounting block and wing support, b) the static test setup with the wing mounted and the propeller in place, c) the propeller tested, and d) a schematic of the static test setup.

hysteresis of 0.02% of rated capacity. Because the tests were performed with the load increasing on the load cell, hysteresis did not limit the accuracy. Nonlinearity is the driving source of error for the load cell and led to a resolution of 0.033 N (0.0075 lbf).

The motor was powered by the Agilent (0–60 V/0–10 A) variable output power supply, which allowed for accurate speed control. The voltage outputs from the torque cell and load cell were sent through the Vishay Measurements 2310 signal conditioning amplifier to a National Instrument BNC-2120 computer interface analog to digital converter and into a computer. The data were then captured using National Instruments LabView™ program. A small piece of reflective tape placed on the propeller provided a signal to a Monarch Model 44 optical tachometer, which was used to verify speed settings. An Extech Instruments phototachometer with an accuracy of 0.05% was also used to provided a dc voltage output to the LabView™ data acquisition system.

The fuselage prototype with adjustable wing placement was placed opposite the propeller and, for most cases, the wing was attached to the fuselage. The thrust line of the propeller was consistently set parallel to the root chord line. The fuselage was affixed to a Modern Machine and Tool six-component balance with a normal load capacity of 44.5 N (10 lbf), an axial capacity of 22.2 N (5 lbf), and a roll-moment capacity of 0.45 N · mm (4 in. · lbf). The balance was required to meet or exceed the specification of 0.5% of full capacity for each component, and the calibration test report from the manufacturer specifies accuracy of 0.010 N (0.002 lbf) for the axial gage, 0.053 N (0.012 lbf) for the normal gage, and 0.50 N · mm (0.0044 in. · lbf) for the roll-moment gage. The balance was mounted on a sting, as depicted in Fig. 2b, and a 5 V power supply excited the balance while the data were conditioned with a National Instruments Model 1314 signal conditioner. Sets of data were collected with the wing mounted at five different axial locations and four different vertical locations relative to the center of the propeller, resulting in 20 positions total. The axial distance (X_o) was measured from the front of the propeller to the leading edge of the wing, whereas the vertical distance (Z_o) was measured from the center of the propeller hub to the leading edge of the wing. A positive Z_o value indicates that the wing is above the propeller, which is the typical arrangement for the aircraft. An important point is that the battery of static tests was conducted without any representation of the tail on the aircraft to isolate propeller–wing interaction.

At each location, data sets consisting of the motor torque and thrust and each of the six balance components were gathered at 8000, 10,000, 12,000, and 13,600 rpm. These propeller speeds correspond to Reynolds numbers based on the length scale of propeller diameter and a tip speed (Re_D) of 2.1×10^5, 2.7×10^5, 3.2×10^5, and 3.7×10^5, respectively. The propeller diameter was selected for the length scale for Reynolds number, but other length scale choices such as tip chord are also sometimes selected, which results in approximately an order of magnitude reduction in the Reynolds number reference value. The rpm values were measured with an optical sensor and are accurate to within 0.05%. At each test point, the torque, thrust, and rpm were measured and time averaged over a 10 s span. At each test point, balance data were also collected for 20–30 s. This allowed time for any vibrations due to the increase in propeller speed to settle out. It also provided enough time to produce adequate data for time-averaged forces and moments.

B. Wind-Tunnel Tests

The purpose of the second phase of testing was to clarify the propeller–airframe interference for a single wing location using velocity measurements. This entailed mounting the wing on the vehicle fuselage in its design location and placing it in the Air Force Institute of Technology's low-speed wind tunnel on the six-degree balance. Because of concerns about flow interference, the separate motor and fuselage mounting configuration of the static test setup was not used for this sequence of tests. Rather, the motor was placed in its customary position at the nose of the aircraft and was operated via a remote control unit. Because of battery life limitations, power was supplied to the motor from a source outside the wind tunnel and care was taken to prevent bias due to forces acting on the electrical connections. The vehicle was mounted on the same tunnel balance used in the static test arrangement. A mounting block placed on the belly of the fuselage was used to accommodate the balance with clearance for the sting. This configuration was also used in [10] and was justified in light of the location of a camera pod of similar dimensions on the flight vehicle. Hot-wire measurements were taken using a triple-wire anemometer to provide velocity profiles of each component at multiple locations about the vehicle. The balance was attached to a sting support that enters the test section from the bottom of the tunnel. The support system includes two stepper motors that enable the wind tunnel article to be positioned with a ± 20 deg angle of attack and a ± 25 deg sideslip angle. Unless otherwise noted, the sting was maintained at an angle of attack of 0 deg, so that the body axes and wind axes were aligned.

To provide velocity profiles around the vehicle, a Dantec Dynamics Streamline anemometer system was used. Velocity and directional calibration of the probe were performed using a 90H10 calibration module with a 90H02 flow unit combined with a nozzle providing a velocity calibration range from 0.5 to 60 m/s. The 55P91 triwire anemometer probe used in the experiments contains three mutually perpendicular gold-plated wires, each 5 μm in diameter and 3.2 mm in length with a sensor length of 1.25 mm. The wires are arranged to an acceptance conical angle of 70.6 deg. When the flow direction is within this conical angle, the direction of the flow can be uniquely resolved. The wire was mounted on rotation stages capable of adjusting the angle through a full rotation about the probe axis and a ± 70 deg sweep through the other two axes, and the calibration was performed according to manufacturer specifications. The data were low-pass filtered, and the acquisition rate was 1 kHz. The accuracy of the same model of triaxial anemometer was addressed by Yeung and Squire [12], who reported that, when the flow vector is within 10 deg of the probe axis, the velocity magnitude can be measured within a confidence limit of $\pm 1\%$ and flow angles could be measured within 2 deg. For cone angles of 20 deg, the maximum velocity percentage error was found by Yeung and Squire to increase to $\pm 3.5\%$, and the maximum flow angularity errors were found to increase to ± 4 deg.

A three-axis traverse was used to position the probe within the tunnel though, for the tests described here, only two axes were used. The probe was inserted into the tunnel through a slot located on the top of the tunnel, and the tip of the anemometer was positioned approximately 1 in. aft of the trailing edge of the wing at the root chord location. The axis of the anemometer was set perpendicular to the streamwise flow direction (u component) in the tunnel, with the tip of the anemometer offset approximately 10 cm from the stem. The presence of the tail downstream of the wire prevented full access to a complete measurement grid, and so as many as five smaller separate grids were used to work the probe around the sting and tail of the vehicle. Because of the physical constraints of the tail and the sting, this resulted in data not being collected at three small areas near the center of the vehicle. A view from aft of the model is given in Fig. 3, in which the test grids are outlined as boxes. The axial position of the probe was held constant at 2.5 cm aft of the root chord of the wing. Velocity and balance data were collected for multiple combinations, including nominal tunnel speeds of 0, 8.2, and 12.2 m/s for the propeller-on and propeller-off cases. The propeller speed was set to 8000 rpm for the propeller-on cases performed in the wind tunnel. Time-averaged results, based on 1024 samples per point, were computed.

III. Results A: Static Propeller/Wing Interactions

The data presented for this study include propeller thrust and torque along with the vehicle lift, drag, and roll moment. A representative portion of a data set for the highest speed setting of 13,600 rpm and fixed Z_0 is included in Table 2 to show the magnitude of the forces in the testing and the limits in the accuracy of the measurements. The drag can be seen to remain relatively constant as the wing is moved progressively closer to the propeller until the wing is positioned at 0.17 D downstream of the propeller, where a nearly

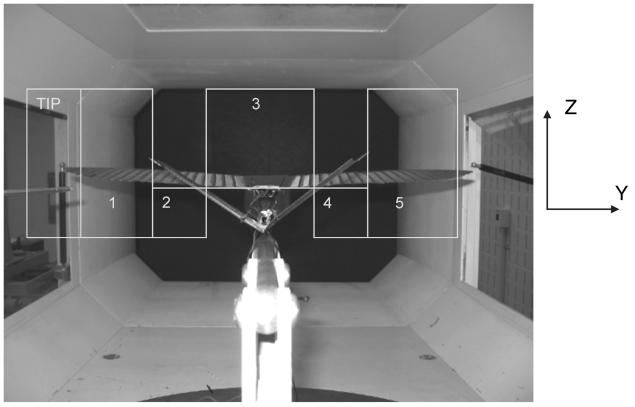

Fig. 3 Hot-wire test grids from the aft view of the vehicle inside the wind tunnel.

20% increase occurred. Interestingly, the roll moment was at a maximum value at the farthest aft wing position, 0.73 D downstream of the propeller. Also, the lift created by the propeller was essentially zero for the propeller locations studied. Propeller thrust remained constant to within the measurement accuracy of the load cell as the wing position changed. These results are generally consistent with those of Witkowski et al., who demonstrated that thrust measurements for a wing with a varied angle of attack relative to the propeller axis had a negligible effect on propeller thrust [3]. Likewise, the torque supplied by the motor to the propeller increased by 1% for the 13,600 rpm case, though the difference in torque was just barely above the accuracy limit of the torque cell. For practical purposes, the propeller alone did not contribute to lift of the wing for the geometries indicated in Table 2, as indicated by values that fell within the error limits of the balance in each instance.

The propeller thrust and torque values in Table 2 lead to a disk loading of 160 N/m^2 and a power loading of 19 W/N. Because the freestream velocity is nominally zero, the propeller efficiency, as conventionally defined for forward flight, would be zero. A figure of merit (FM), which is commonly used for rotorcraft, of 0.42 can be determined using the convention described in [13] with the equation given in Eq. (1):

$$\mathrm{FM} = \frac{[T/(\rho N^2 D^4)]^{3/2}}{\sqrt{2} \times (Q/\rho N^2 D^5)} \tag{1}$$

This value is low compared with typical values reported for large-scale rotors. However, the value is reasonably close to the low Reynolds number data reported in [14], in which a propeller-tip Reynolds number of the same order of magnitude results in a maximum figure of merit ranging between 0.35 and 0.53.

Nondimensional values of drag/thrust (D/T) and roll moment/motor reaction torque (ℓ/Q) also provide insight when comparing different test conditions. Figure 4a shows the effect of propeller speed on the value of D/T for different wing placement, whereas Fig. 4b provides a contour representation of D/T. In this figure, the 10,000 rpm data are used in the contour plot, but it can be seen from the line plots that the propeller speed had little influence on the D/T ratio within the speed range tested. In each of these plots, the x axis shows the axial distance between the wing and propeller, the different line styles represent the height of the leading edge of the

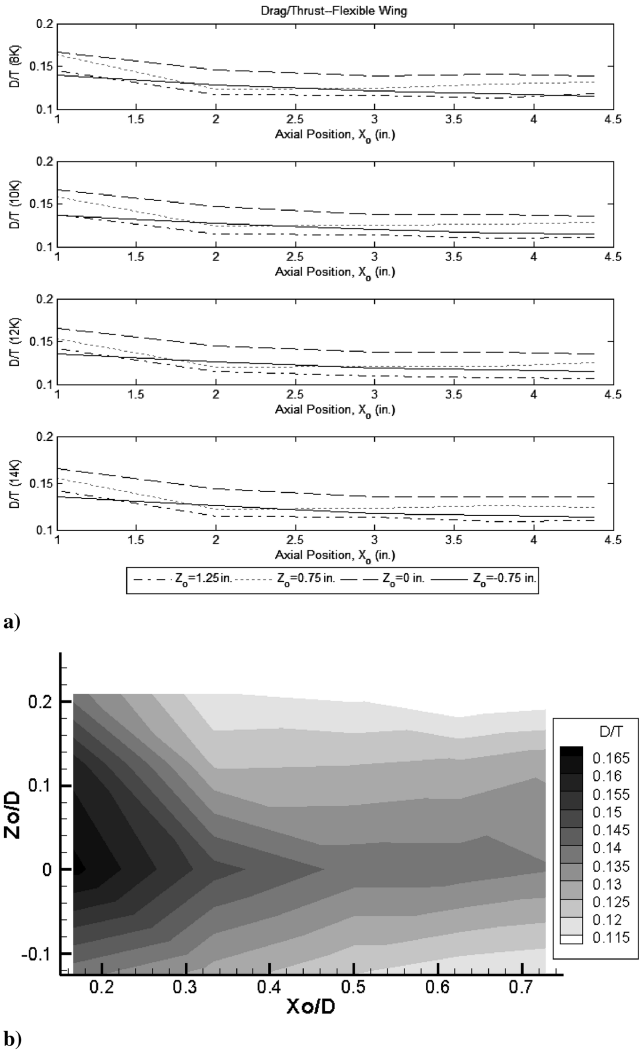

Fig. 4 Shown are the following: a) drag-to-thrust curves for varied motor speeds, and b) a contour map for a propeller speed of 10,000 rpm for a varied wing location.

wing with respect to the propeller, and the negative values indicate the wing below the propeller. The data collected for $X_o/D = 0.73$ closely represent the design location of the wing, and so the lower values of X_o provide insight into the effect of moving the wing closer to the propeller. Figure 4a shows that the propeller speed has little influence on the overall behavior of D/T. By contrast, there is a clear increase in D/T as the wing approaches the vicinity of the propeller, particularly when the wing is placed within 0.33 D of the propeller. The data in Table 2 demonstrate that this effect is primarily due to an increase in drag and that thrust is relatively unaffected by the presence of the wing. Generally speaking, the farther the wing is from the propeller, both in the X_o and Z_o directions, the less drag per unit thrust on the vehicle.

The fact that there is variance in the drag but little measured change in the thrust is an indication that the relatively low Reynolds number may be playing a role in the behavior of the propeller–wing interaction. The stagger theorem of Munk, which is based on an

Table 2 Forces and moments acquired from the static test apparatus for $N = 13,600$ rpm

Axial location X_o/D	Vertical location Z_o/D	Lift, N	Drag, N	Roll moment,ℓ, N · mm	Thrust, N	Propeller torque, Q, N · mm
0.73	0.21	-0.002 ± 0.05	0.324 ± 0.010	15.7 ± 0.5	2.92 ± 0.03	39.7 ± 0.2
0.62	0.21	-0.022 ± 0.05	0.323 ± 0.010	14.3 ± 0.5	2.94 ± 0.03	40.1 ± 0.2
0.5	0.21	-0.047 ± 0.05	0.336 ± 0.010	13.3 ± 0.5	2.95 ± 0.03	40.3 ± 0.2
0.33	0.21	-0.036 ± 0.05	0.337 ± 0.010	13.8 ± 0.5	2.92 ± 0.03	40.1 ± 0.2
0.17	0.21	-0.009 ± 0.05	0.423 ± 0.010	14.4 ± 0.5	2.97 ± 0.03	40.5 ± 0.2

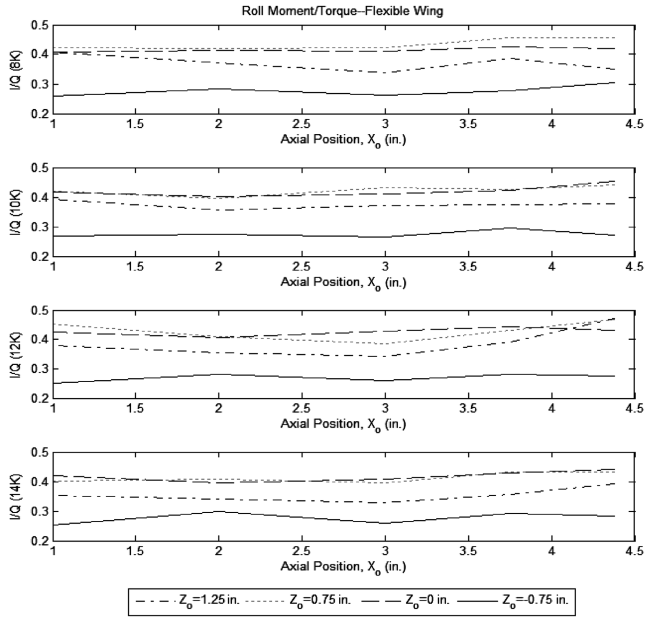

a)

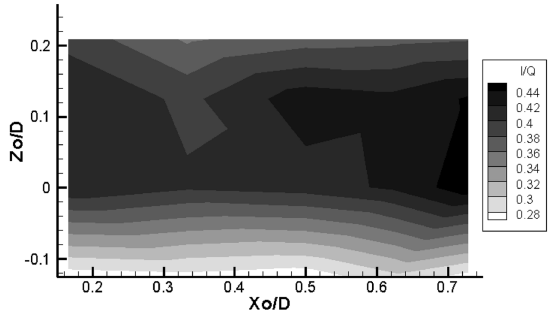

b)

Fig. 5 Shown are the following: a) roll moment to torque curves for varied motor speeds, and b) a contour plot for a motor speed of 10,000 rpm for a varied wing location.

inviscid flow assumption and is often applied to propeller–wing combinations, suggests that "the net axial force is independent of the streamwise position of surfaces with a given circulation distribution [15]." These measurements for varied streamwise positions suggest that the Reynolds number regime for the operating environment for the BATCAM does result in small deviations from the inviscid theory.

A second nondimensional value of importance is the roll moment/motor reaction torque (ℓ/Q). In the static testing configuration, the roll moment is induced only by the propeller wake on the wing as the wing acts to straighten the circumferential flow generated by the propeller. The data in Fig. 5a show the effect of propeller speed on ℓ/Q, whereas Fig. 5b provides a contour plot representation of ℓ/Q for the 10,000 rpm case. Although the curves change slightly for different rpm settings, there are no pronounced trends with the propeller speed evident in Fig. 5a. By contrast, wing placement, in particular, the vertical offset dimension Z_o, does influence the magnitude of this term. Interestingly, the design location ($X_o/D = 0.73$, $Z_o/D = 0.21$) essentially gave the maximum value for ℓ/Q among the data acquired, as indicated in Fig. 5b. The tabulation of data for a single speed in Table 3 demonstrates that the changes in the roll-moment values, rather than motor torque, are primarily responsible for the changes in the ratio of ℓ/Q for constant propeller speed, as the position of the wing is changed from its station above the propeller axis ($Z_0/D = 0.21$) to a location below the propeller axis ($Z_0/D = -0.12$).

The resulting contour plot of the ratio of roll moment to torque shows that the value reaches a local minima near $X_0/D = 0.3$ and is largest at the farthest downstream wing position. This stands in contrast to the drag-to-thrust data, which decreased monotonically. One possible explanation is that the local minima might be associated with the contraction of the cross section of the propeller slipstream. Veldhuis presents a derivation of the diameter of the slipstream in the vena contract region for a propeller, absent a nacelle, in [16] for an inviscid flow, neglecting swirl. It is conceivable that the anticipated decrease in the radius of the slipstream could be offset by the mixing and entrainment of ambient air into the stream, leading to the local minima in the drag-to-thrust ratio. Some insight into the behavior of the flowfield was gained through the hot-wire anemometry experiments.

IV. Results B: Wind-Tunnel Velocity Profiles and Balance Data

The separation of the motor from the fuselage and flexible wing could not be easily implemented in the wind tunnel due to interference and blockage effects of the support, the thrust table, and the torque cell. Rather, in the wind tunnel, a conventional sting-mounted six-component balance model test was used to collect data. Therefore, the aircraft and propeller thrust are combined into a single reading, and the motor torque and reaction roll moment are combined into a single reading.

Limited propeller performance data were gathered by collecting measurements on the vehicle with the wing removed from the fuselage. Here, the roll-moment measurement is roughly equivalent to the motor torque, and the negative axial force, taring axial load values for a zero-propeller-speed case, can be treated as the thrust. This approach does not account for any reaction roll moment or drag brought about by the interaction of the propwash with the fuselage and tail, which is likely to introduce a small bias toward lower readings for both the propeller torque and thrust. Nevertheless, it does provide useful information on the propeller performance for the test conditions. The propeller data presented in Fig. 6 were taken with the tunnel operated at 7.9 m/s, and propeller speed was varied from 8150 to 10,600 rpm.

Conditions under which data were acquired and axial force readings from the six-component balance are listed in Table 4. The balance data corresponding to the tests were time averaged and corrected for sensor interactions. Note that, for each data point presented, the body axes and wind axes were aligned. Detailed velocity profiles were collected for a variety of circumstances to provide added insight into the distribution of forces acting on the aircraft. Data for the tests conducted in the wind tunnel include all three components of velocity and reaction forces and moments on the vehicle with the wing placed at its design location ($X_o/D = 0.73$, $Z_o/D = 0.21$).

A comparison of the first two rows shown in Table 4 is consistent with the results of the static bench testing in that the placement of the wing in its design location reduces the total axial force (i.e., the difference between drag and thrust) by roughly 10%. The conditions

Table 3 Forces and moments measured using the static test stand at 13,600 rpm at varied vertical propeller locations

Axial location X_o/D	Vertical location Z_o/D	Lift, N	Drag, N	Roll moment, N · mm	Thrust, N	Propeller torque, N · mm
0.73	0.21	-0.002 ± 0.05	0.324 ± 0.010	15.7 ± 0.5	2.92 ± 0.03	39.7 ± 0.2
0.73	0.12	-0.007 ± 0.05	0.351 ± 0.010	17.6 ± 0.5	2.81 ± 0.03	40.6 ± 0.2
0.73	0	0.101 ± 0.05	0.390 ± 0.010	18.0 ± 0.5	2.88 ± 0.03	40.7 ± 0.2
0.73	−0.12	0.172 ± 0.05	0.319 ± 0.010	11.5 ± 0.5	2.80 ± 0.03	40.4 ± 0.2

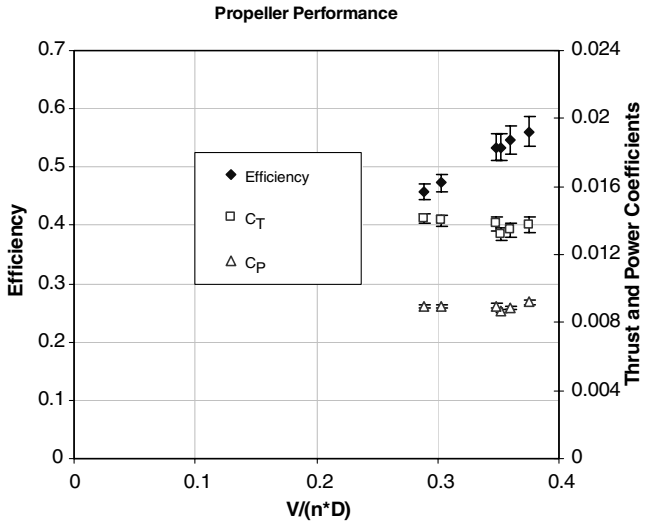

Fig. 6 Propeller thrust coefficient, power coefficients, and efficiency for a fixed tunnel speed (7.9 m/s) and varied propeller speed.

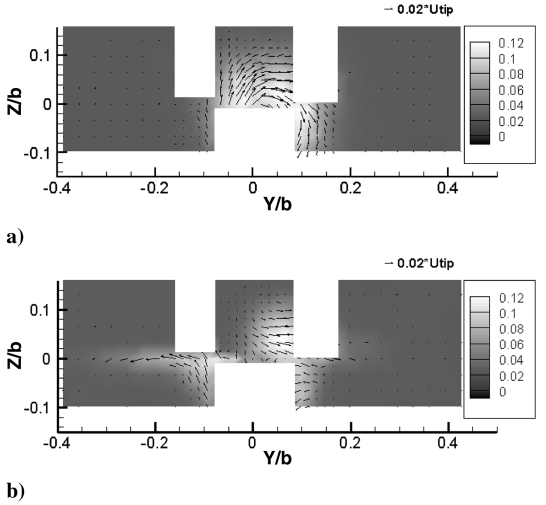

Fig. 7 Velocities for the propeller-on (8000 rpm), zero freestream cases: a) fuselage without a wing, and b) fuselage with the wing mounted. Contours are shown for streamwise velocities, and vector plots of secondary flows are both normalized by propeller-tip speed.

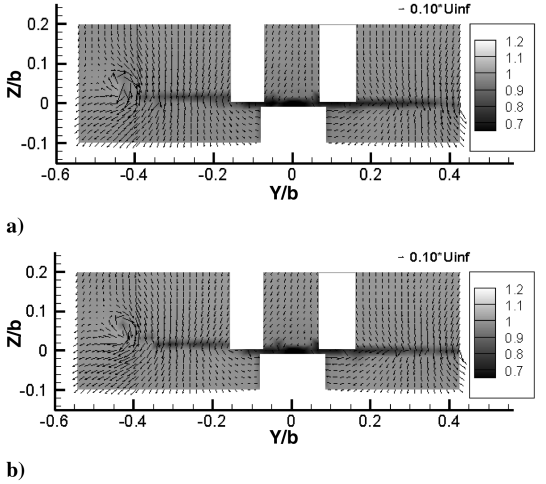

Fig. 8 Velocity profiles for propeller-off cases: a) $Re_c = 0.85 \times 10^5$ (8.2 m/s), and b) $Re_c = 1.3 \times 10^5$ (12.2 m/s).

indicated in the second row would be consistent with the conditions for the aircraft at the initiation of takeoff. The conditions represented in the third and fourth rows are generally consistent with two different airspeeds experienced in a glide condition though, in the wind-tunnel tests, the propeller was removed from the aircraft. The fifth row is consistent with conditions during acceleration, whereas the sixth and final row of Table 4 would be consistent with conditions at steady level flight, assuming that the aircraft weight was fully offset by the lift acting on the aircraft. The far right column of Table 4 references Figs. 7–9, which contain velocity maps corresponding to each condition. The streamwise velocities for different test conditions are given in the form of contours, and vectors representing secondary velocities are superimposed onto each plot. All the velocity components are presented in meters per second. Each legend shows a representative 1 m/s length vector. The white areas of the contour plots indicate areas that could not be reached by the probe due to interference with the model.

The velocity data for data sets acquired with a propeller speed set at 8000 RPM and the wind-tunnel motor off are given in Fig. 7. Because the wind-tunnel velocity was nearly zero, all the velocities are normalized by the propeller-tip speed. The contours represent normalized streamwise velocities, whereas the vectors represent the secondary velocity components, also normalized by tip speed. Figure 7a shows the propeller flow with the wing removed, whereas Fig. 7b shows the distorted propwash with the addition of the wing. From the vantage point aft of the vehicle looking upstream, the air in the propeller wake rotates clockwise and reaches axial velocities of 8 m/s. The axial velocity component is largest at a point above and to the right of the center of the propeller and decays outward in a radial fashion. Interestingly, at the axial plane of the test, which is almost 2 propeller diameters (0.28 m) aft of the propeller, the propwash extends outward only about 25% more than the physical diameter of the propeller.

The radial extent of the propeller slipstream, absent the wing, may be estimated from the location at which the velocity is midway between the peak velocity and the ambient velocity. As shown in Fig. 7a, this location is approximately 1.05 D along the horizontal propeller axis, whereas the radius of the idealized inviscid slipstream would be expected to monotonically decrease with distance from the propeller [16]. This lends some credence to the notion that viscous mixing of the slipstream and the ambient flow is influencing the ratio of roll moment to propeller torque. A comparison of Figs. 7a and 7b clearly demonstrates how the secondary flow patterns within the propeller wake are influenced by the wing under conditions emulating takeoff. Starting with the top center of the propeller wake, the flow rotates clockwise until it comes into proximity with the upper surface of the right wing, where it begins to move outward toward the wing tip. This creates the downward force on the right

Table 4 Wind tunnel conditions for measurements, $\alpha = 0$

Wind tunnel airspeed, m/s	Wing configuration	Propeller configuration	Total axial force measured, N (drag–thrust)	Velocity representation
0	Off	8000 rpm	−1.14	Figure 7a
0	On	8000 rpm	−1.03	Figure 7b
8.2	On	Off	0.16	Figure 8a
12.2	On	Off	0.35	Figure 8b
8.2	On	8000 rpm	−0.41	Figure 9a
12.2	On	8000 rpm	−0.003	Figure 9b

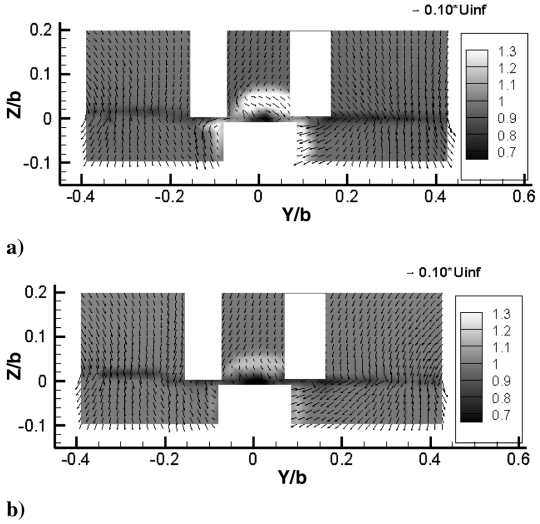

Fig. 9 Velocities for a powered propeller (8000 rpm): a) $Re_c = 0.85 \times 10^5$ (8.2 m/s freestream velocity), and b) $Re_c = 1.3 \times 10^5$ (12.25 m/s freestream velocity).

wing as indicated by the static test results. Below the right wing, the flow moves toward the center of the aircraft. Under the left wing and close to the fuselage, the flow is directed toward the wing and then is forced toward the left wing tip. Collectively, the net effect of the wing can be considered, in light of the static bench tests, as countering the torque applied to the aircraft by the motor.

Figure 8 shows the velocity profiles at two different freestream conditions where the propeller has been removed from the aircraft. Figure 8a corresponds to the $Re = 0.85 \times 10^5$ (8.2 m/s freestream) test condition, whereas Fig. 8b corresponds to the 1.3×10^5 (12.2 m/s freestream) test condition. In these data sets, a slightly larger interrogation region led to the detection of tip vortices, consistent with the positive lift generated by the wing on the aircraft. Aside from the wing-tip vortices, the flow is largely aligned in the axial direction for both cases. The wake region of the wing due to the buildup of a boundary layer on its surface is the dominant feature in the central portion of both plots.

As one would expect, the addition of the propeller operating at 8000 rpm substantially changes the velocity profile, as shown in Fig. 9, in which each velocity component is normalized by the freestream velocity as opposed to the propeller-tip speed. The most obvious change is the addition of the propeller wake creating a large u component near the center of the vehicle as indicated by the larger velocities reflected in the contour levels. It appears that the effect of the propeller on the secondary velocity components is combined with the tunnel freestream velocity; its effect is not quite as pronounced. The axial component has a maximum increase of just over 3 m/s with the addition of the propeller in the nominal 8.2 m/s case shown in Fig. 9a, whereas it created over 8 m/s of flow with no freestream, as can be seen in Fig. 7b. The circular region of the propeller wake is still highly recognizable, especially near the longitudinal axis of the aircraft; however, the effect of the wing on the propwash is considerably less pronounced.

The velocity data collected for a nominal tunnel setting of 12.2 m/s, which coincided with a nearly zero reading in total axial force, are given in Fig. 9b. An increase of approximately 2 m/s over the freestream velocity is seen in the vicinity of the propwash. The difference in the conditions with respect to the freestream can be seen in the contour maps. In both plots, the wake region of the wing is evident and is largely unaffected by the propeller except for regions very close to the center portion of the aircraft. Figure 9, like Fig. 7, does not contain the full extent of the wing. Given the character of the secondary flow in the region shown, however, it is unlikely that the propeller had any substantial influence on the wing-tip region.

The radial extent of the slipstream may also be analyzed by once again considering the location at which the velocity is midway between its maximum value and its value in the freestream. For the conditions represented in both Figs. 7a and 7b, this distance is approximately 0.9 D, with differences between the two being difficult to detect given the spatial resolution of the measurements. For both conditions, however, this value is considerably smaller the 1.05 D value found for the wing-off condition in Fig. 7a. This suggests that the mixing rate is measurably reduced as the ratio of the slipstream velocity to the ambient velocity is reduced (i.e., as the freestream velocity increases).

The wing placement is such that a positive lift is present when the reference value used for α is set to 0. The vehicle was characterized in previous studies as having a C_L of 0.7 at $\alpha = 0$ deg [10]. Therefore, it is not surprising that there is a small downward velocity component present in the vector maps. However, it should also be noted that we believe that there is a small bias due to a small nonzero probe insertion angle.

In addition to the work performed characterizing the propeller–wing interaction region, the hot-wire probe was traversed in the wing-tip region to characterize the tip vortex of the port wing. In part, these data were collected as a means of confirming the data collection method, but the velocity information gathered is also of general interest and is worthy of discussion. The data were collected for a range of α from 0 to 10 deg. The lift coefficient values were checked during the series of experiments and closely matched the archival data acquired for the vehicle [10].

Velocity data acquired for varied angle-of-attack settings aft are given in Fig. 10. In each set of measurements, the data were acquired in a plane normal to the streamwise direction with the tunnel freestream velocity of 12.25 m/s, resulting in a Reynolds number, based on the mean chord, of 1.3×10^5. The 5 mm grid spacing resolved the wing-tip vortex, and the peak streamwise velocity was found to increase in the vortex core. The largest secondary velocity within the vortex was found to be consistent with an approximately 30 deg cone angle. It is noteworthy that the physical wing tip has a Y coordinate of 305 mm, whereas the vortex core is centered roughly around 265 mm, in other words, at 87% of the half-span. An increase in streamwise velocity has been documented in archival publications, with peak velocity ranging from as low as 1.06 to as high as 1.78 times the freestream velocity with a dependence on a circulation parameter ($\Gamma/U_\infty b$) [17]. Here, this value, which was calculated directly from lift force, varies from 0.05 at $\alpha = 0$ deg to 0.11 for the $\alpha = 10$ deg case. In this series of tests, the peak streamwise velocity ranges from 1.04 to 1.16 times the freestream velocity, and only a small influence due to α and, therefore, the circulation parameter, $\Gamma/U_\infty b$, was detected. As a point of comparison, Anderson and Lawton acquired three-component hot-wire anemometry data for a symmetric wing and found a strong dependence on the circulation parameter [18]. In terms of magnitude, they reported an increase in velocity of approximately 20% of the freestream when a flat wing tip was used with their configuration. The magnitudes we measured on our small air vehicle compare reasonably well in terms of magnitude, though no clearly defined dependence on the circulation parameter was found in our study. In addition to the peak velocity in the vortex core, the velocity deficit behind the wing is clearly present, which is consistent with viscous effects. Note that the angle reference used both herein and in [10] results in a positive lift coefficient at a nominal angle of attack of 0 deg. Reynolds number effects may obscure trends relating the peak streamwise velocity and the vortex circulation parameter. The effect of separated flow on the wing is particularly evident in the low velocity region of the $\alpha = 10$ deg data given in Fig. 10f. The highest angle-of-attack case also exhibits a reduction in the peak streamwise velocity in the core of the wing-tip vortex.

V. Conclusions

A series of experiments incorporating both load and velocity measurements were conducted, with the primary goal of illuminating the propeller–wing interaction for a specific miniature air vehicle, a version of BATCAM. A static test stand incorporated a six-component balance and a separate torque and thrust measurement system to collect data on the motor and wing separately. These results

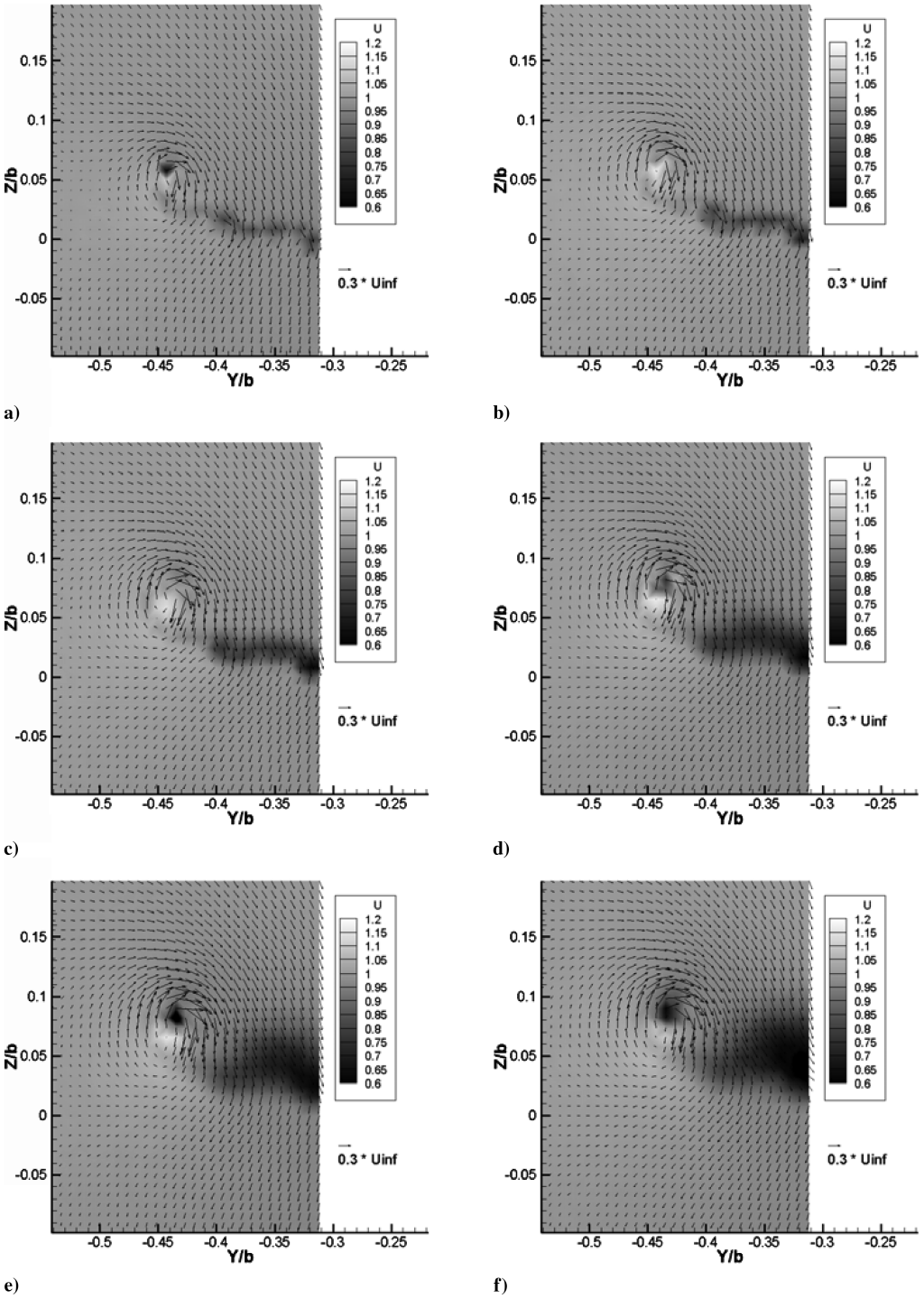

Fig. 10 Velocity for a varied angle of attack for the propeller-off configuration for $U_{\text{inf}} = (Re_c = 1.3 \times 10^5)$: a) $\alpha = 0$ deg and $C_L = 0.7$, b) $\alpha = 2$ deg and $C_L = 0.9$, c) $\alpha = 4$ deg and $C_L = 1.1$, d) $\alpha = 6$ deg and $C_L = 1.2$, e) $\alpha = 8$ deg and $C_L = 1.3$, and f) $\alpha = 10$ deg and $C_L = 1.3$. Secondary flow vectors are overlaid onto the contours of streamwise velocity, each normalized by the freestream velocity (12.2 m/s).

show the effect of positioning the wing relative to the propeller under zero freestream conditions. At the design location, the drag was found to be approximately 11% of the thrust, whereas the roll moment was 38% of the motor torque. The drag on the fuselage and wing was seen to increase to a value of 16% of the thrust, whereas the roll moment increased slightly to 39% of the motor torque for a wing placement of 0.17 D from the propeller. For a fixed propeller speed, the torque on the motor was only minimally affected by the axial wing placement and, somewhat surprisingly, yielded a minimum value at about 0.5 D when the vertical design location was used. The ratio of motor torque to the roll moment was found to be more influenced by the wing's vertical position than by the axial position and reached values as high as 0.44 for the case in which the propeller axis and chord lines closely aligned. Drag, as a percentage of thrust, also increased to a maximum when the wing was at this same vertical location.

Traditional six-component balance measurements were also collected in a wind tunnel for both propeller-on and propeller-off conditions at typical aircraft operating conditions. The velocity profiles 1 in. downstream of the wing root were collected using three-component hot-wire velocimetry, and the effect of the wing on the propeller wake was made evident by streamwise velocity contours and secondary velocity vector maps. Axial force data collected at a reference angle of attack of 0 deg were used to determine accelerating and steady flight conditions for a propeller-on (8000 rpm) condition, whereas a propeller-off case was used to characterize a glide

condition. As freestream velocity increases, the effect of the wing on the secondary velocity components is more difficult to discern. The hot-wire data indicated a low-velocity region consistent with boundary-layer effects in the wake of the wing for both the propeller-off and powered runs.

A fine mesh of velocity data was acquired in the vicinity of the wing-tip vortex for a varied angle of attack. The vortex was clearly mapped and was found to be centered at 0.87 times the wing half-span. These data indicated an increase in the streamwise velocity near the vortex core to a value of up to 1.16 times that of the freestream. These results are comparable to values found in the literature for wings of similar loading. However, in contrast to some published results on wing-tip vortices generated by rigid wings with a well-defined airfoil section, there was no clear trend in the behavior of the peak streamwise velocity within the vortex core as the angle of attack increased.

Acknowledgments

The authors are grateful for the support of the U.S. Air Force Research Laboratory and specifically for the assistance provided by Greg Parker and Michael Ol of the Air Vehicles Directorate and Gregg Abate of the Munitions Directorate. The views expressed in this article are those of the authors and do not reflect the official policy or position of the U.S. Air Force, the Department of Defense, or the U.S. Government.

References

[1] Kuhn, R., "Investigation of the Effects of Ground Proximity and Propeller Position on the Effectiveness of a Wing with Large-Chord Slotted Flaps in Redirecting Propeller Slipstreams Downward for Vertical Take-Off," NACA, Technical Note 3629, Langley Aeronautical Laboratory, Langley Field, VA, 1956.

[2] Hayes, W. C., Kuhn, R. E., Sherman, I. R., "Effects of Propeller Position and Overlap on the Slipstream Deflection Characteristics of a Wing-Propeller Configuration Equipped with a Sliding and Fowler Flap," NACA, Technical Note 4404, Langley Aeronautical Laboratory, Langley Field, VA, 1958.

[3] Witkowski, D. P., Lee, A. K. H., and Sullivan, J. P., "Aerodynamic Interaction Between Propellers and Wings," *Journal of Aircraft*, Vol. 26, No. 9, 1989, pp. 829–836. doi:10.2514/3.45848

[4] Bi, N. P., and Leishman, G., "Experimental Study of Rotor/Body Aerodynamic Interactions," *Journal of Aircraft*, Vol. 27, No. 9, 1990, pp. 779–788. doi:10.2514/3.45938

[5] Favier, D., Ettaouil, A., and Maresca, C., "Numerical and Experimental Investigation of Isolated Propeller Wakes in Axial Flight," *Journal of Aircraft*, Vol. 26, No. 9, 1989, pp. 837–846. doi:10.2514/3.45849

[6] Chiaramonte, J., Favier, D., Maresca, C., and Benneceur, S., "Aerodynamic Interaction Study of the Propeller/Wing Under Different Flow Conditions," *Journal of Aircraft*, Vol. 33, No. 1, 1996, pp. 46–52. doi:10.2514/3.46901

[7] Fratello, G., Favier, D., and Maresca, C., "Experimental and Numerical Study of the Propeller/Fixed Wing Interaction," *Journal of Aircraft*, Vol. 28, No. 6, 1991, pp. 365–373. doi:10.2514/3.46036

[8] Ardito Marretta, R. M., "Different Wings Flowfields Interaction on the Wing-Propeller Coupling," *Journal of Aircraft*, Vol. 34, No. 6, 1997, pp. 740–746. doi:10.2514/2.2252

[9] Janus, J. M., "General Aviation Propeller-Airframe Integration Simulations," *Journal of Aircraft*, Vol. 43, No. 2, 2006, pp. 390–394. doi:10.2514/1.15354

[10] DeLuca, A. M., Reeder, M. F., Freeman, J., and Ol, M. V., "Flexible- and Rigid-Wing Micro Air Vehicle: Lift and Drag Comparison," *Journal of Aircraft*, Vol. 43, No. 2, 2006, pp. 572–576. doi:10.2514/1.15643

[11] Gamble, B., "Experimental Analysis of Propeller Interactions with a Flexible Wing Micro-Air-Vehicle," M.S. Thesis, Department of Aeronautics and Astronautics, Air Force Institute of Technology, Wright–Patterson Air Force Base, OH, 2006.

[12] Yeung, C. P., and Squire, L. C., "Numerical Calibration and Verification Tests of an Orthogonal Triple-Hot-Wire Probe," *Measurement Science and Technology*, Vol. 4, No. 12, Dec. 1993, pp. 1446–1456. doi:10.1088/0957-0233/4/12/022

[13] Leishman, J. G., *Principles of Helicopter Aerodynamics*, Cambridge Univ. Press, Cambridge, England, U.K., 2000, ISBN 0-521-66060-2.

[14] Young, L. A., Aiken, E., Johnson, J. L., Demblewski, R., Andrews, J., Klem, J., "New Concepts and Perspectives on Micro-Rotorcraft and Small Autonomous Rotary-Wing Vehicles," AIAA Paper 2002-2816, 2002.

[15] Kroo, I., "Propeller-Wing Integration for Minimum Induced Loss," *Journal of Aircraft*, Vol. 23, No. 7, 1986, pp. 561–565. doi:10.2514/3.45344

[16] Veldhuis, L., "Propeller-Wing Aerodynamic Interference," Ph.D. Dissertation, Department of Aerospace Engineering, Delft University of Technology, 2005, ISBN 90-9019537-8.

[17] Spalart, P. R., "Airplane Trailing Vortices," *Annual Review of Fluid Mechanics*, Vol. 30, Jan. 1998, pp. 107–138. doi:10.1146/annurev.fluid.30.1.107

[18] Anderson, E. A., and Lawton, T. A., "Correlation Between Vortex Strength and Axial Velocity in a Trailing Vortex," *Journal of Aircraft*, Vol. 40, No. 4, 2003, pp. 699–704. doi:10.2514/2.3148